

Article

# A Study on Surface Modification Characteristics and Charge–Discharge Mechanism of Natural Serpentine Ore Secondary Battery

Jun-Ren Zhao <sup>1</sup>, Kuan-Jen Chen <sup>2</sup> , Fei-Yi Hung <sup>1,\*</sup> , Yung-Yi Tsai <sup>1</sup> and Po-Ting Wu <sup>1</sup>

<sup>1</sup> Department of Materials Science and Engineering, National Cheng Kung University, Tainan 70101, Taiwan; a2x346yz03@gmail.com (J.-R.Z.); hi6900347@hotmail.com.tw (Y.-Y.T.)

<sup>2</sup> Department of Mechanical Engineering, Southern Taiwan University of Science and Technology, Tainan 710, Taiwan; kjchen@stust.edu.tw

\* Correspondence: fyhung@mail.ncku.edu.tw; Tel.: +886-6-2757575-62950

**Abstract:** This study conducts low-vacuum sulfidation to form a sulfidation layer on the serpentine-derived magnesium iron silicate, thereby enhancing its electrochemical properties. Results show (Mg,Fe)<sub>2</sub>SiO<sub>4</sub> calcined at 900 °C has the best crystallinity, and the cubic FeS<sub>2</sub> is synthesized on the surface of the orthorhombic magnesium iron silicate (MFS). Two distinct charge plateaus can be distinguished during the first charge process, and the discharge capacities increased significantly. This study confirms that the surface FeS<sub>2</sub> layer provides extra ion pathways, allowing more lithium/magnesium ions to be extracted and inserted in the serpentine-derived magnesium iron silicate. Accordingly, the serpentine electrode boasts straightforward exploitation with low-cost advantages and potential.

**Keywords:** ore battery; serpentine; magnesium iron silicate; sulfidation; charge–discharge



**Citation:** Zhao, J.-R.; Chen, K.-J.; Hung, F.-Y.; Tsai, Y.-Y.; Wu, P.-T. A Study on Surface Modification Characteristics and Charge–Discharge Mechanism of Natural Serpentine Ore Secondary Battery. *Inorganics* **2024**, *12*, 13. <https://doi.org/10.3390/inorganics12010013>

Academic Editor: Qingguo Shao

Received: 25 November 2023

Revised: 23 December 2023

Accepted: 25 December 2023

Published: 27 December 2023



**Copyright:** © 2023 by the authors. Licensee MDPI, Basel, Switzerland. This article is an open access article distributed under the terms and conditions of the Creative Commons Attribution (CC BY) license (<https://creativecommons.org/licenses/by/4.0/>).

## 1. Introduction

Lithium-ion batteries (LIB) currently dominate the secondary battery market, finding extensive use in portable electronic devices and electric vehicles. In anticipation of future energy demand and increasingly stringent safety standards, sodium-ion batteries (NIB) and magnesium-ion batteries (MIB) are emerging as potential alternatives [1–3]. Notably, metallic magnesium, in comparison to metallic lithium, boasts a lower cost, abundant reserves, and a higher theoretical volume energy density [4,5]. Moreover, magnesium exhibits enhanced safety characteristics, featuring a higher melting point, inertness in air, and resistance to dendrite formation during repeated cycles. Additionally, multivalent-ion batteries like magnesium-ion batteries offer a higher volumetric energy density compared to monovalent-ion batteries, including lithium-ion and sodium-ion batteries [6]. As a result, MIB has garnered widespread attention in recent years. The potential advantages of MIB, encompassing safety, cost effectiveness, and energy density, position it as a promising candidate for the evolving landscape of energy storage technologies.

Polyanionic compounds (XO<sub>4</sub><sup>n-</sup>, X = P, Si, Ge, etc.) have demonstrated excellent reversible Li<sup>+</sup> insertion/extraction [7,8]. And orthosilicates are capable of stabilizing the crystal lattice during charge–discharge and generating relatively high operating voltages owing to the strong Si–O bonds and strong inductive effect [9]. Among the orthosilicates, olivine-type (Mg,M)<sub>2</sub>SiO<sub>4</sub> (M = Fe, Mn, Co) has been successfully used as cathode material in MIBs [10–12]. In view of the high theoretical capacity exceeding 300 mAh/g and high operating voltage relative to conventional Mg-ion battery cathodes, (Mg,M)<sub>2</sub>SiO<sub>4</sub> is a promising cathode material for rechargeable Mg-ion batteries. According to previous studies [10,12,13], (Mg,M)<sub>2</sub>SiO<sub>4</sub> can be successfully synthesized through the solid-state method, sol–gel method or molten salt method, and demonstrates reversible Mg<sup>2+</sup> insertion/extraction processes.

Serpentinite is a hydrated, magnesium-rich silicate mineral, classified as a metamorphic rock with the chemical formula  $\text{Mg}_3\text{Si}_2\text{O}_5(\text{OH})_4$ . This unique mineral exhibits several distinctive characteristics: (1) Surface appearance: natural serpentinite has a glossy, dark green appearance (green iron ore). It is recognizable by its snakeskin-like textures, hard texture, and is widely used in building materials. (2) Chemical composition: serpentinite comprises various minerals, including plagioclase, hornblende, olivine, and others such as pyroxene, chlorite, and mica. (3) Material characteristics: ranging of Mohs Hardness from about 2.5 to 4.0, serpentinite is classified as a relatively soft mineral; contains metallic elements; and demonstrates electrical conductivity. The electrical properties of serpentine ore depend on its mineral composition and crystal structure. Being typically non-conductive or possessing low conductivity, serpentinite exhibits relatively high resistance to the passage of current. When serpentine ore contacts an electrode, an electrochemical reaction occurs on the surface, leading to a polarization effect. This effect finds applications in both scientific and industrial contexts [14].

Due to the major component in serpentinite being  $(\text{Mg,Fe})_3\text{Si}_2\text{O}_5(\text{OH})_4$ , serpentine undergoes dehydration and recrystallization reactions, and thereby transforms into  $(\text{Mg,Fe})_2\text{SiO}_4$  after high temperature calcination. Moreover, serpentinite is an abundant non-toxic and low-cost mineral. Therefore, it is reasonable to evaluate the feasibility of synthesizing Mg-ion cathode material  $(\text{Mg,Fe})_2\text{SiO}_4$  from serpentinite. On the other hand, it is well known that coating conductive materials onto an active material enhances the rate-capability and cycling stability [15].

The thermal phase transformation of serpentine to form magnesium silicate is a topotactic reaction, requiring a clear azimuthal relationship. According to the literature [14], the dehydration reaction and recrystallization reaction of serpentine can be written as Equations (1) and (2).



During the thermal dehydration process of serpentine at 100–700 °C, surface atoms absorb significant heat, resulting in rapid water removal and causing atomic arrangements to become disordered. This high atomic disorder leads to a lower recrystallization reaction rate at 700–810 °C compared to the interior. The resulting low surface crystallinity renders it unsuitable for secondary batteries, as it fails to provide sufficient ion channels, leading to a gram capacitance that deviates from the theoretical capacitance. Additionally, the magnetite ( $\text{Fe}_3\text{O}_4$ ) originally present in the serpentinite undergoes phase transformation at 250–550 °C and 650–850 °C, sequentially forming maghemite ( $\gamma\text{-Fe}_2\text{O}_3$ ) and hematite ( $\alpha\text{-Fe}_2\text{O}_3$ ). Hematite, being the main component of rust, exhibits poor electrical conductivity. Hence, the primary focus of this research is the preparation of magnesium iron silicate with both surface crystallinity and electrical conductivity.

Sulfur, an abundant and environmentally friendly element on Earth, stands out for its non-toxicity and affordability. It holds great promise in both lithium-ion and magnesium-ion batteries, offering high capacity and energy density. Additionally, most metal sulfides exhibit the dual advantages of high capacitance and good conductivity. The electrochemical properties of intercalation compound electrodes are intricately linked to their conductivity. Coating the surface with a material of excellent conductivity can enhance capacitance and cycle stability under high-current discharge. Therefore, sulfidation is anticipated to address ion conductivity limitations observed in magnesium iron silicate.

Motivated by these considerations, our study involved sulfidation of serpentinite (O-material) to produce  $(\text{Mg,Fe})_2\text{SiO}_4$ , forming a sulfidation layer on the surface to enhance its conductivity. Beyond exploring charge–discharge behaviors, this research delved into sulfidation mechanisms. The findings hold significant potential as valuable references for the industry, contributing to the development of more efficient and sustainable energy storage solutions.

## 2. Experimental Procedure

### 2.1. Preparation of MFS-H and MFS-S Powders

Magnesium iron silicate (MFS) was prepared by calcination. First, serpentinite was ground with a grinding machine at a rate of 60 rpm for 10 min and its median diameter  $D_{50}$  was controlled to below 50  $\mu\text{m}$ . The resultant powder was named as O-material (without any treatment). To obtain MFS, two kinds of calcination atmospheres were adopted: (1) calcination in air, (2) calcination in a sulfur atmosphere. For calcination in air, the O-material was heated in air at different temperatures (700, 800 and 900  $^{\circ}\text{C}$ ) for 1 h, and named as MFS-H-700, MFS-H-800 and MFS-H-900, respectively. For the other method, O-material was mixed with pure sulfur powder (1:3 mass ratio) and fired in a low-vacuum tube furnace ( $10^{-1}$  atm) at the same three temperatures (700, 800 and 900  $^{\circ}\text{C}$ ) for 1 h. The obtained products were labeled as MFS-S-700, MFS-S-800 and MFS-S-900, respectively.

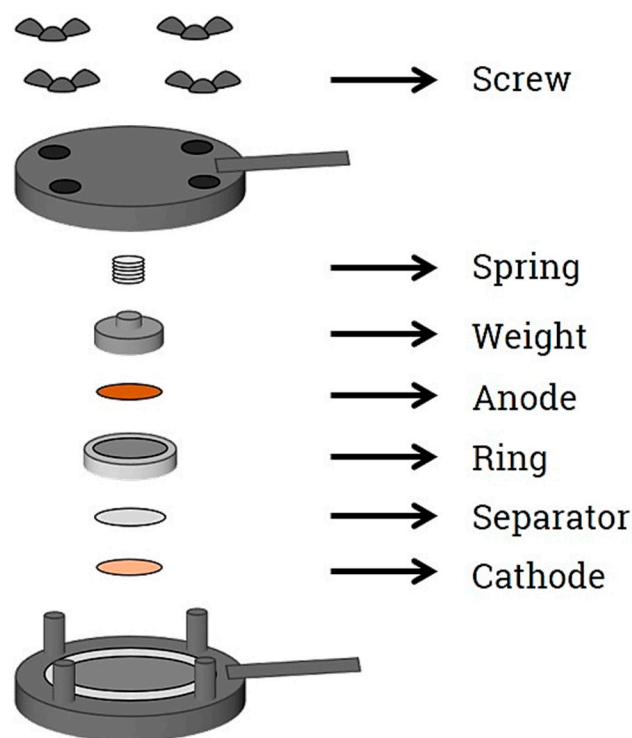
### 2.2. Structural and Morphological Characterization

Crystalline phases of the samples in the matrix were identified by a Bruker D8 Discover X-ray diffraction (XRD) instrument operating at 40 kV and 40 mA with Cu  $K\alpha$  radiation ( $\lambda = 0.154184$  nm) at a rate of  $3^{\circ}/\text{min}$  from  $20^{\circ}$  to  $80^{\circ}$  ( $2\theta$  range).

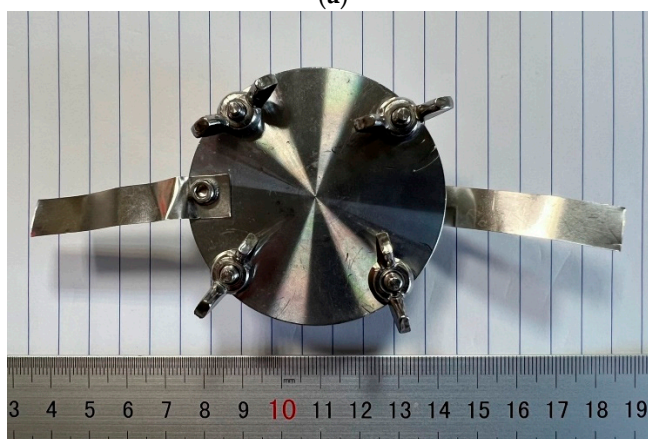
Fourier transform infrared spectroscopy (FTIR, Perkin Elmer C88323, Waltham, MA, USA) was used to detect powder characteristics. To understand the phase structure, transmission electron microscopy (TEM, Tecnai G2 F20 S-TWIN, Hillsboro, OR, USA) equipped with selected area electron diffraction (SAED) was used. Field emission scanning electron microscopy (FE-SEM, ZEISS AURIGA, Jena, Germany) equipped with energy dispersive spectroscopy (EDS) was employed to observe the surface morphologies of the particles and detect the chemical composition. Thickness of the sulfidation layer was determined by Auger electron spectroscopy (AES, VG Scientific, MICROLAB 350, Imberhorne Lane, United Kingdom) coupled with argon etching. The primary electron acceleration voltage was 10 keV, while the acceleration voltage and the beam current of argon ion beam for etching were 3 kV and 19  $\mu\text{A}/\text{cm}^2$ , respectively.

### 2.3. Electrochemical Measurements

The electrochemical performance was evaluated by using HA-cells (Figure 1) [13,16]. The working electrodes were first prepared by mixing 80 wt.% active materials, 10 wt.% polyvinylidene fluoride (PVDF, dissolved in N-methyl-2-pyrrolidone solvent) and 10 wt.% carbon black. After mixing, the slurry was loaded onto Al foil serving as a current collector and dried at 60  $^{\circ}\text{C}$  for 12 h; then, it was cut into discs with a diameter of 13 mm and further dried at 100  $^{\circ}\text{C}$  for 12 h under vacuum. Thereafter, the HA-cells were assembled in a Ar-filled glove box with metallic lithium foil as the counter electrode, 1.0M  $\text{LiPF}_6$  dissolved in a mixture of EC/PC/DMC (3:1:6,  $v/v$ ) as the electrolyte and with a polypropylene separator. Charge–discharge tests were examined in the potential range of 1.0–3.0 V via a multichannel battery analyzer. The current density was 0.02  $\text{mA}/\text{cm}^2$  and the test temperatures were room temperature (25  $^{\circ}\text{C}$ ) and high temperatures (55, 65 and 75  $^{\circ}\text{C}$ ). Owing to the relatively low specific capacities, we only conducted charge–discharge tests for 10 cycles. Electrochemical impedance spectra (EIS, PARSTAT2273) analysis was performed by applying 10 mV amplitude with a frequency range from 10 Hz to 100 kHz. Furthermore, the  $\text{Mg}^{2+}$  extraction amounts of MFS-H-900 and MFS-S-900 after the initial charge process were analyzed by an inductively coupled plasma optical emission spectrometer (ICP-OES, Varian VISTA-MPX, Palo Alto, CA, USA).



(a)



(b)

Figure 1. BT-Cell: (a) internal structure and (b) appearance.

### 3. Results and Discussion

#### 3.1. Morphology and Structure

The morphologies of the natural serpentinite ore in Figure 2 and MFS particles displayed irregular shapes, with the average diameter ( $D_{50}$ ) of the MFS-H-900 and MFS-S-900 particles measured at 87 and 85  $\mu\text{m}$ , respectively (Figure 3). In Figure 4, the elemental mapping of MFS-S-900 powder is depicted. Notably, the position of the sulfur signal aligns consistently with the scattered positions of magnesium, silicon, oxygen, and iron atoms. This alignment suggests the uniform formation of the sulfur-containing phase generated by sulfide sintering on the surface of MFS-S-900 powder. Additionally, experimental observations revealed that an increase in the vulcanization sintering temperature corresponds to a color change in the powder, transitioning from light green to dark green.



Figure 2. Natural serpentinite ore and grinding powders.

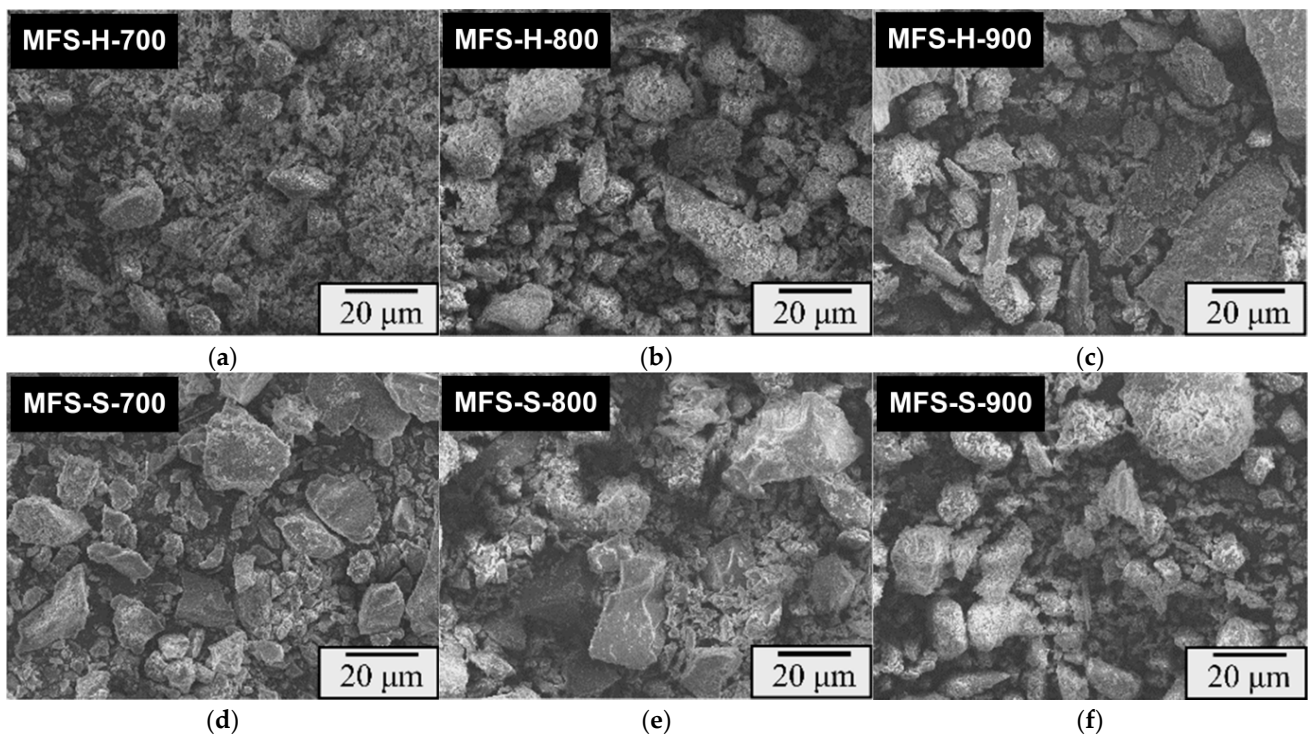
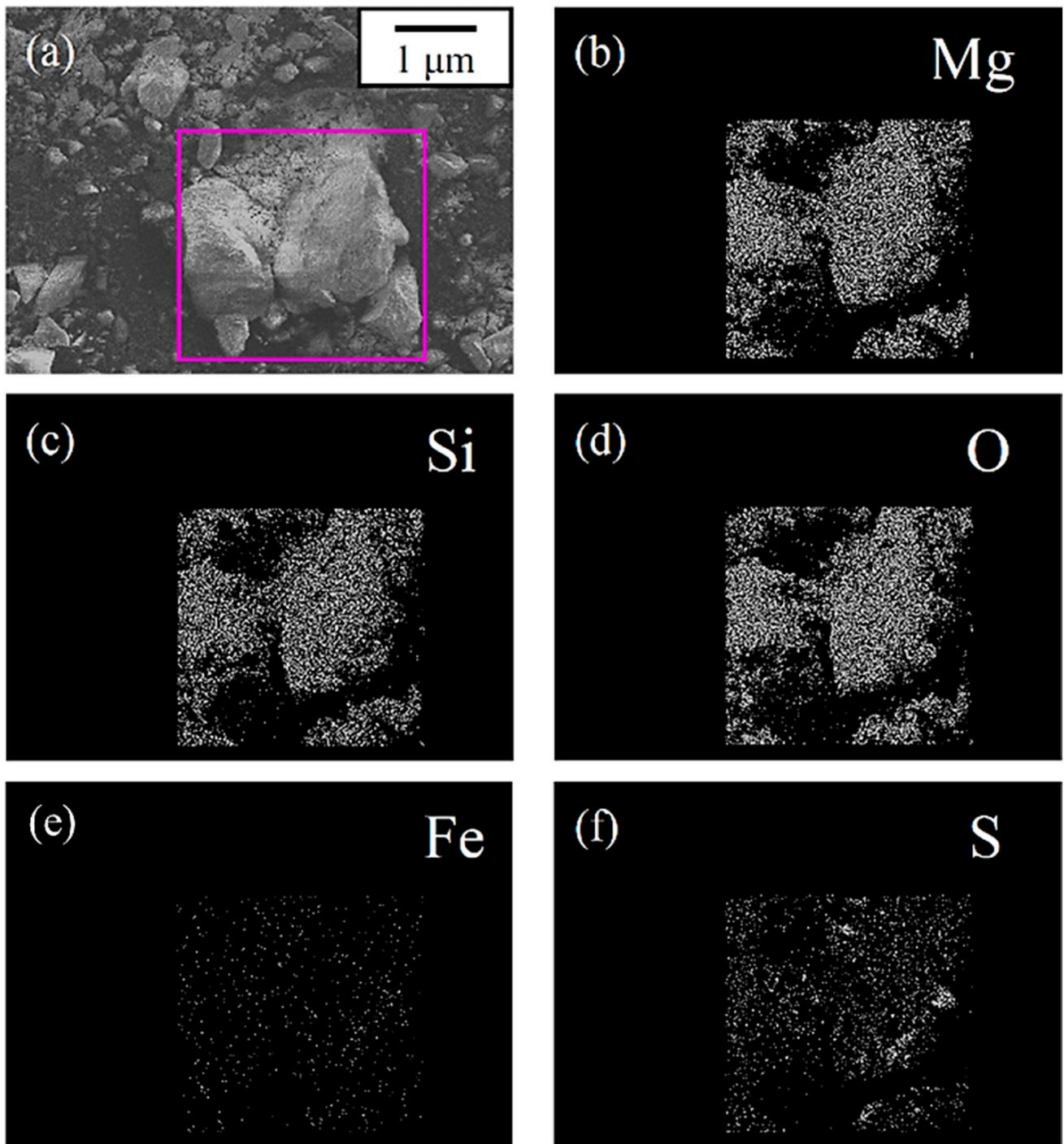


Figure 3. Microstructure of powders: (a) MFS-H-700, (b) MFS-H-800, (c) MFS-H-900, (d) MFS-S-700, (e) MFS-S-800, (f) MFS-S-900.



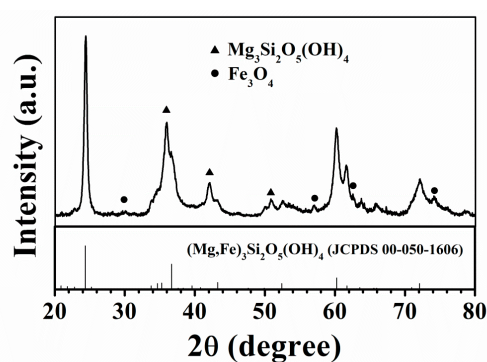
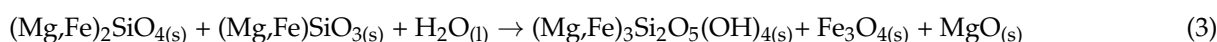
**Figure 4.** (a) SEM image, and EDS mapping of (b) Mg, (c) Si, (d) O, (e) Fe, and (f) S in MFS-S-900 particle.

Compared with the O-material, the MFS particle size increased with increasing temperature due to high-temperature solid-state reactions. The chemical components of the MFS-S particles are shown in Table 1. The elements ratio of all particles are roughly in accordance with the chemical composition of  $(\text{Mg,Fe})_2\text{SiO}_4 + (\text{Mg,Fe})\text{SiO}_3$ . Note that the sulfur content is invariable with increasing temperature, which indicates that sulfide formed uniformly on the MFS-S particle surface.

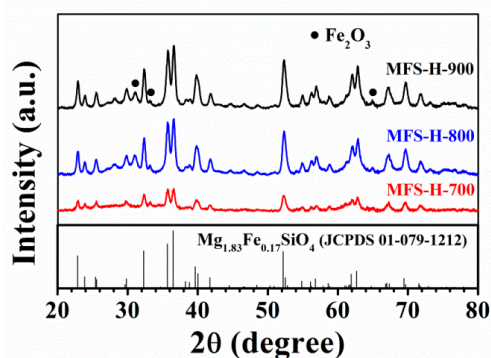
**Table 1.** Chemical composition of MFS-S particles.

Element (at.%)	Mg	Si	Fe	O	S
MFS-S-700	19.89	14.82	2.77	62.18	0.34
MFS-S-800	21.22	15.95	3.31	59.09	0.43
MFS-S-900	20.55	15.49	2.18	61.47	0.31

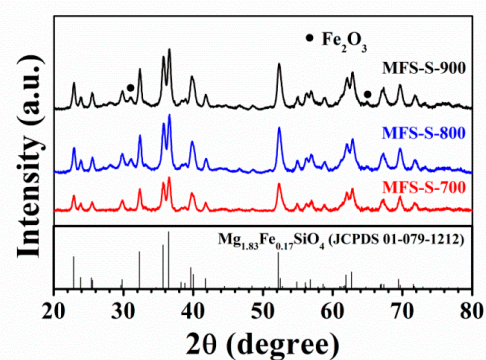
Figure 5a shows the XRD pattern of the O-material, the diffraction peaks of which can be indexed to  $(\text{Mg,Fe})_3\text{Si}_2\text{O}_5(\text{OH})_4$  (JCPDS card No: 00-050-1606),  $\text{Mg}_3\text{Si}_2\text{O}_5(\text{OH})_4$  (JCPDS card No: 01-072-1500) and  $\text{Fe}_3\text{O}_4$  (JCPDS card No: 01-071-6336).  $\text{Fe}_3\text{O}_4$  is the byproduct in the serpentinization reaction, which can be written as Equation (3) [17]:



(a)



(b)

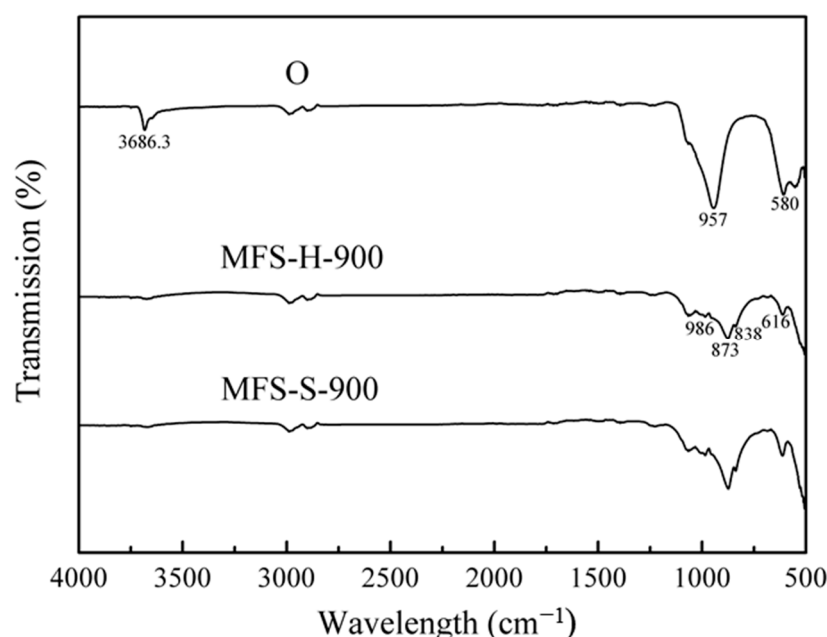


(c)

**Figure 5.** X-ray diffraction patterns: (a) O-material, (b) MFS-H, (c) MFS-S particles.

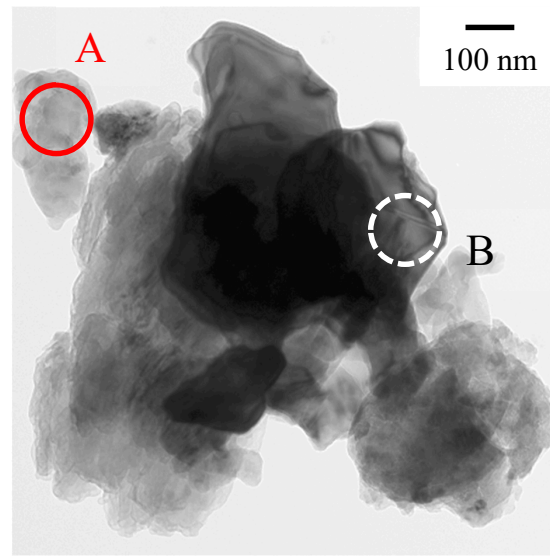
In Figure 5b,c, the XRD patterns of MFS-H and MFS-S particles show that the peaks sharpen with increasing temperature, indicating that the crystallinity of the magnesium iron silicate enhances in this temperature range. All the diffraction peaks are well indexed to orthorhombic  $\text{Mg}_{1.83}\text{Fe}_{0.17}\text{SiO}_4$  (JCPDS card No: 01-079-1212 and  $a = 4.76 \text{ \AA}$ ,  $b = 10.22 \text{ \AA}$ ,  $c = 5.99 \text{ \AA}$ ) and hexagonal  $\alpha\text{-Fe}_2\text{O}_3$  (JCPDS card No: 40-1139 and  $a = 5.92 \text{ \AA}$ ,  $c = 35.69 \text{ \AA}$ ), which is derived from phase transformation of  $\text{Fe}_3\text{O}_4$  at 650–850 °C [18]. Absence of sulfide diffraction peaks in the XRD patterns suggests that the sulfide content is too low to be detected by X-ray. Although the diffraction peaks are indexed to JCPDS card No: 01-079-1212 (the orthorhombic  $\text{Mg}_{1.83}\text{Fe}_{0.17}\text{SiO}_4$ ), with the increase in sintering temperature, the diffraction peak shifts slightly to a lower  $2\theta$  angle (Figure 5b,c). This shift indicates an increase in the lattice parameter of magnesium iron silicate. According to the study by Jia et al. [19], this transformation may be attributed to the partial replacement of the original ions by larger ions. In this study, the original Si ions were partially replaced by Fe ions.

Figure 6 presents the FTIR spectra of the O-material, MFS-H-900, and MFS-S-900. In the O-material, the peaks at  $3686.3 \text{ cm}^{-1}$ ,  $957 \text{ cm}^{-1}$ , and  $580 \text{ cm}^{-1}$  correspond to the Mg-OH stretching vibration, Si-O stretching vibration, and Mg-OH bending vibration, respectively, aligning with the serpentine curve. For MFS-H-900, the peaks at  $986 \text{ cm}^{-1}$ ,  $873 \text{ cm}^{-1}$ , and  $838 \text{ cm}^{-1}$  represent the stretching vibration frequencies of  $\text{SiO}_4$  bonding, while the peak at  $616 \text{ cm}^{-1}$  corresponds to the bending vibration frequency of  $\text{SiO}_4$  bonding. Notably, the curve of MFS-H-900 is indistinguishable from that of MFS-S-900, suggesting that sulfide sintering does not induce changes in the chemical bonds.



**Figure 6.** FTIR of serpentinite ore, MFS-H-900 and MFS-S-900 particles.

To confirm the mechanism of sulfidation in the MFS particles, the MFS-S-900 particles are conducted to TEM analysis (Figures 7 and 8). In the TEM bright-field image of the MFS-S-900 particles, EDS analysis was performed on the two selected areas of A and B. The diffraction patterns of selected-area A can be indexed to  $\text{Mg}_{1.83}\text{Fe}_{0.17}\text{SiO}_4$ , which corresponds with the XRD patterns. The diffraction patterns of selected-area B can be indexed to cubic  $\text{FeS}_2$  (JCPDS card No: 00-042-1340 and  $a = b = c = 5.42 \text{ \AA}$ ), indicating that the sulfide in MFS-S lattice is pyrite. In brief, sulfur exists in the form of  $\text{FeS}_2$  in the MFS-S particles.



at. %	Mg	Si	Fe	O	S
A: (Mg, Fe) <sub>2</sub> SiO <sub>4</sub>	25.32	17.15	2.31	54.39	0.83
B: FeS <sub>2</sub>	0.35	0.74	33.45	2.25	63.20

Figure 7. TEM specimen and EDS results of MFS-S-900 particles.

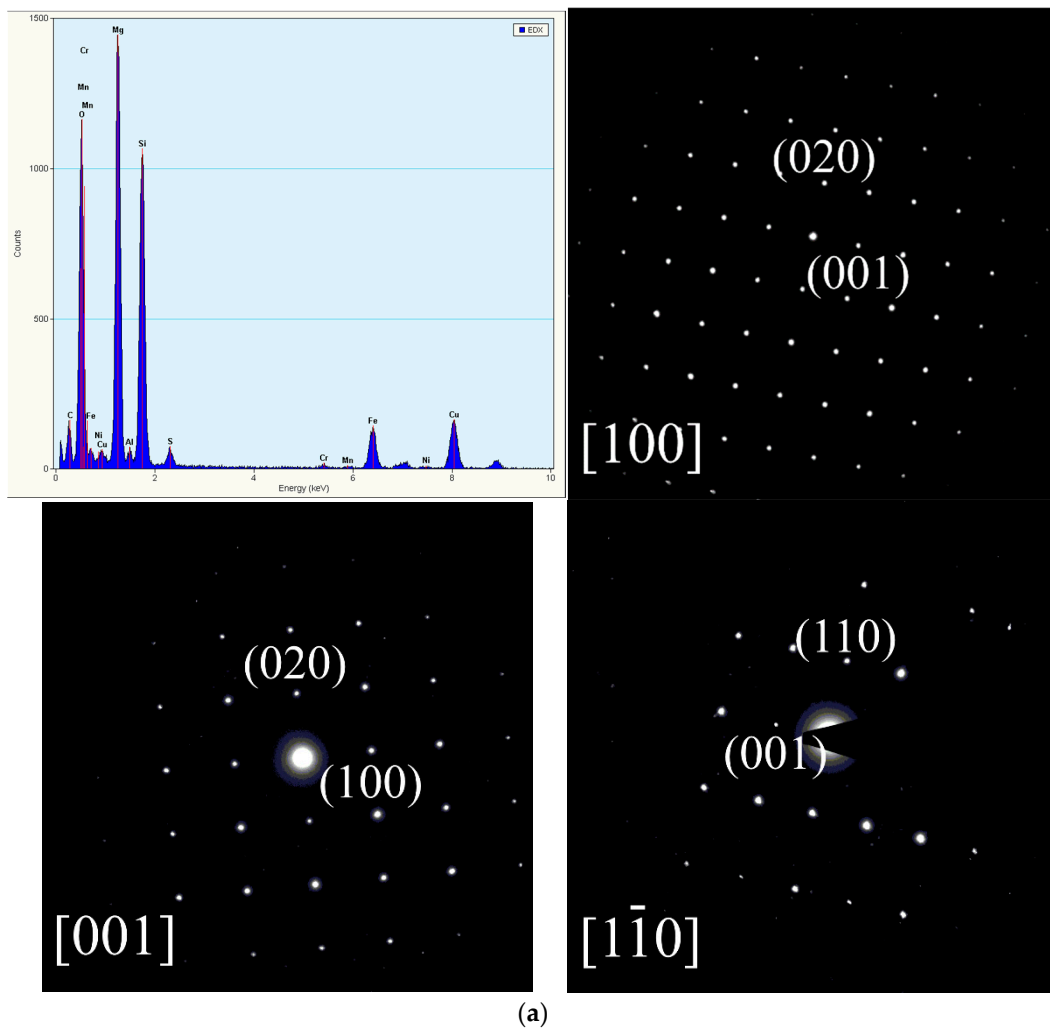
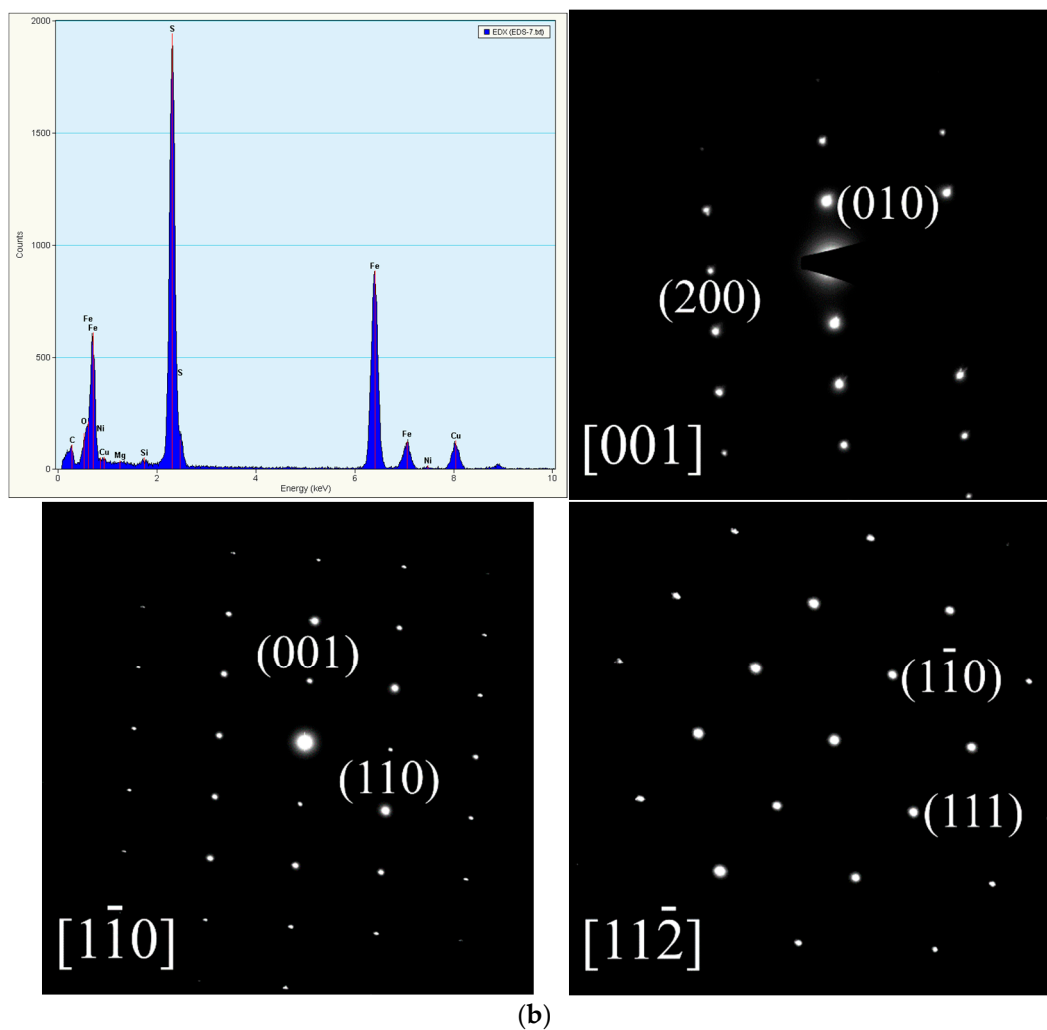
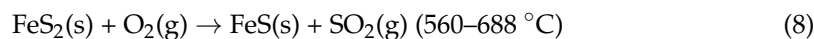
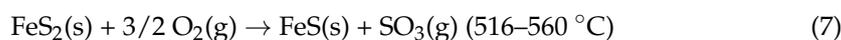
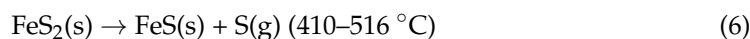
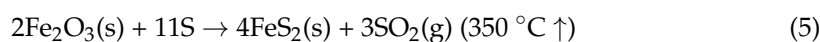
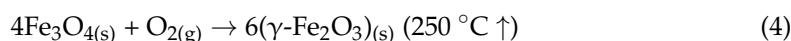


Figure 8. Cont.



**Figure 8.** TEM analysis of MFS-S-900 particles for selected area diffraction pattern: (a) A: (Mg, Fe)<sub>2</sub>SiO<sub>4</sub> (b) B: FeS<sub>2</sub>.

The sulfidation layer thickness was further confirmed by elemental depth profile using an AES. The concentration of sulfur atoms decreases with increase in sputtering time, and the sulfur signal is not detected after sputtering time for 120 s (Figure 9). This indicates the sulfidation layer was approximately 20 nm from the MFS-S particle surface, and like the core-shell structure (Figure 10). Moreover, the sulfur concentration is dependent on the iron concentration, but the Fe/S ratio was not 1:2. This phenomenon suggests that the Fe source for forming pyrite is Fe<sub>3</sub>O<sub>4</sub> near the serpentine crystals rather than ferrous iron doping to serpentine. As mentioned above, it confirmed that the sulfidation layer was composed of pyrite and deduced the pyrite formation reactions Equations (4)–(9) as follows [18,20–25]:



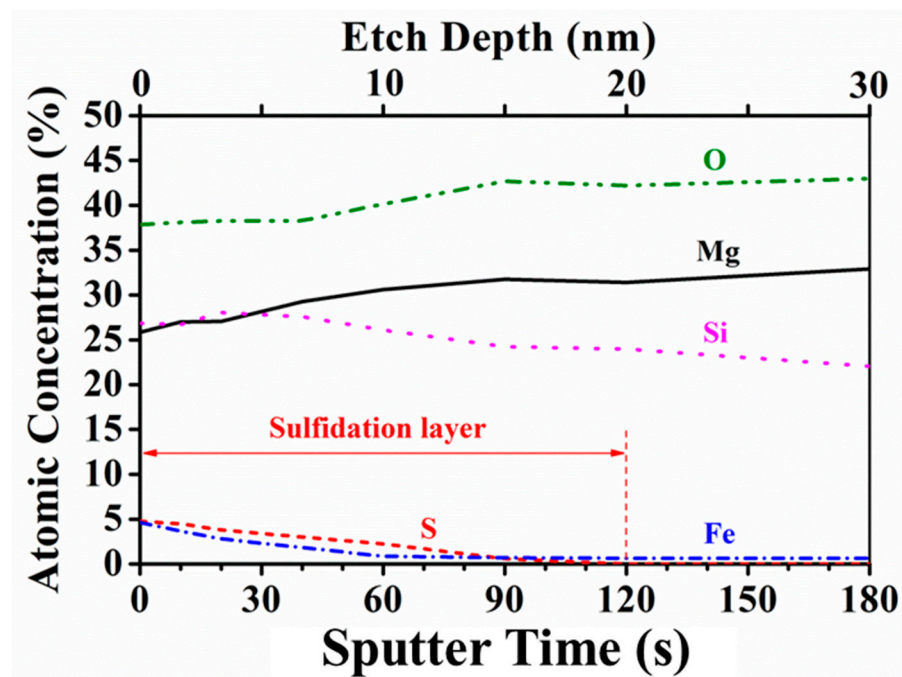


Figure 9. AES elemental depth profile of MFS-S-900 particle.

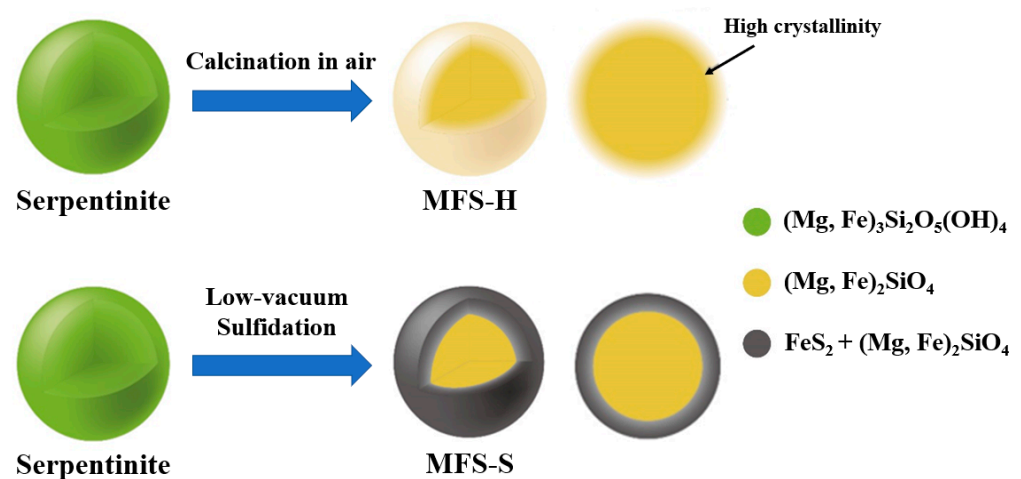


Figure 10. Surface modification characteristics of MFS-S-900 particle.

Natural serpentinite is mainly composed of magnesium iron silicate hydroxide and transforms to magnesium iron silicate with a  $\text{FeS}_2$  sulfidation layer after calcination with sulfur.

### 3.2. Electrochemical Properties

The initial discharge curve of the O-material has a specific capacity of 5.86 mAh/g. However,  $(\text{Mg, Fe})_3\text{Si}_2\text{O}_5(\text{OH})_4$  is not an active material in lithium-ion batteries; as such, the specific capacity is attributed to  $\text{Fe}_3\text{O}_4$  (the theoretical capacity of  $\text{Fe}_3\text{O}_4$  is 926 mAh/g). Figure 11 displays initial charge–discharge curves of the MFS-H-900 and MFS-S-900 at room temperature, and their electrolytes after charging were used to examine the  $\text{Mg}^{2+}$  concentration by ICP-OES, the corresponding results of which are shown in Table 2. The MFS-S-900's electrolyte detected  $\text{Mg}^{2+}$  ions with a concentration of 611 ppb after the first charge, but the MFS-H-900's electrolyte could not detect the presence of  $\text{Mg}^{2+}$  ions. Based on the initial charge–discharge curves for MFS-H-900 and MFS-S-900, the first charge curve of MFS-S-900 has two distinct charge plateaus at about 2.4 and 2.8 V. This indicates that

Mg<sup>2+</sup> ions of (Mg, Fe)<sub>2</sub>SiO<sub>4</sub> in the MFS-S-900 lattice are extracted into an electrolyte in two steps during the initial charge process.

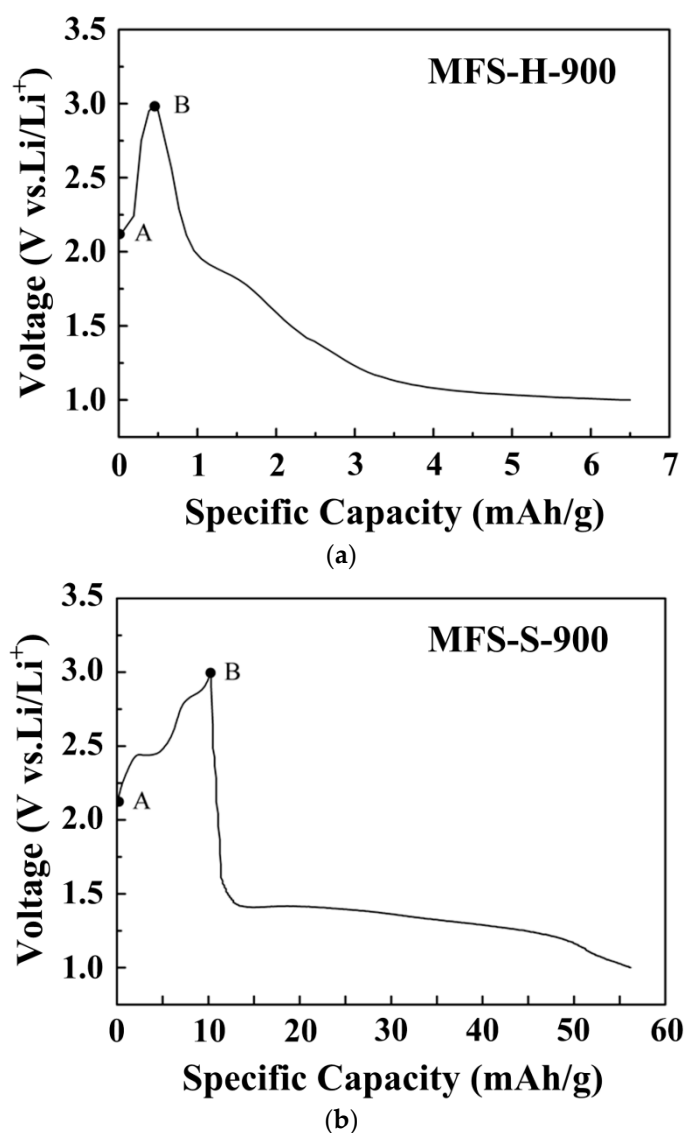


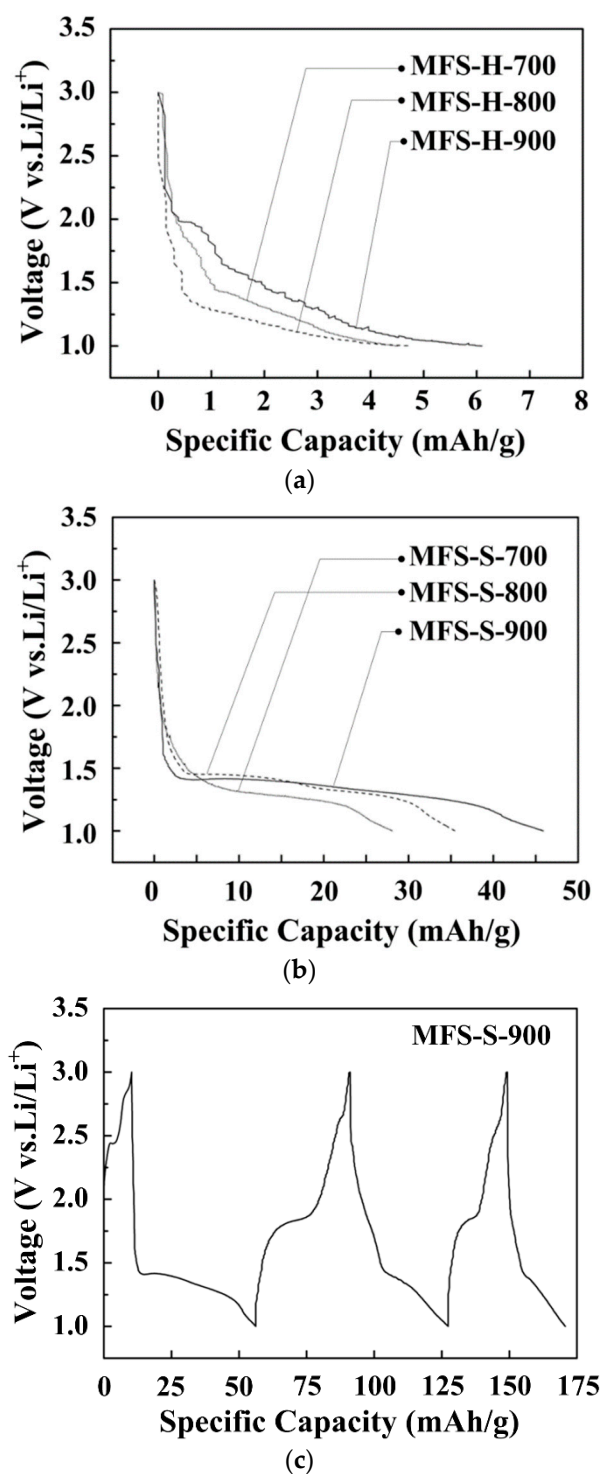
Figure 11. Initial charge–discharge curves: (a) MFS-H-900, (b) MFS-S-900.

Table 2. ICP results of MFS-H-900 and MFS-S-900 powder electrolytes.

Categories	MFS-H-900	MFS-S-900
[Mg <sup>2+</sup> ] (ppb)	N.D.	611

The initial discharge curves of the MFS-H and MFS-S with different sintered temperatures are shown in Figure 12. The initial discharge capacity of MFS-H-700 is 4.7 mAh/g, including the contribution of Fe<sub>2</sub>O<sub>3(s)</sub>, and the specific capacities of MFS-H slightly increase with an enhance in crystallinity. This result confirms that (Mg, Fe)<sub>2</sub>SiO<sub>4</sub> lattices can store a few Li ions. In addition, the phase transformation from serpentine to magnesium silicate can be divided into the dehydration and recrystallization. The recrystallization reaction is a topotactic reaction, which means that the external layer of the particles is hindered by the disorder resulting from the rapid dehydration reaction [26]. Therefore, the amorphous surface of MFS-H is responsible for its poor electrochemical properties. The initial

discharge capacities of MFS-S-700, MFS-S-800 and MFS-S-900 are 28.1, 35.6 and 46 mAh/g, respectively.

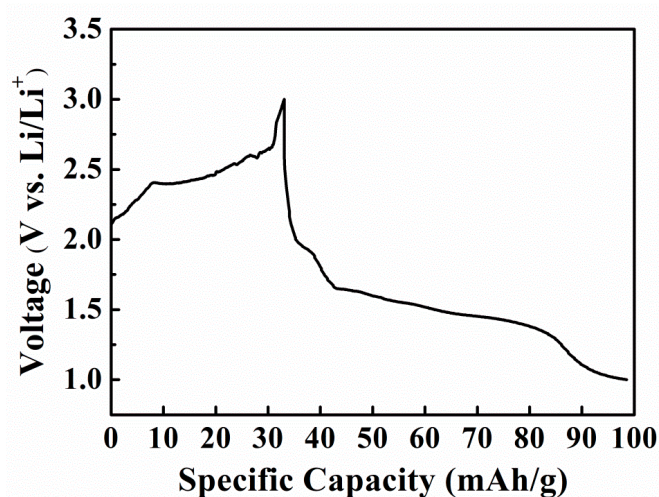


**Figure 12.** Initial discharge curves: (a) MFS-H, (b) MFS-S with different temperatures, (c) charge–discharge cycle curve of MFS-S-900.

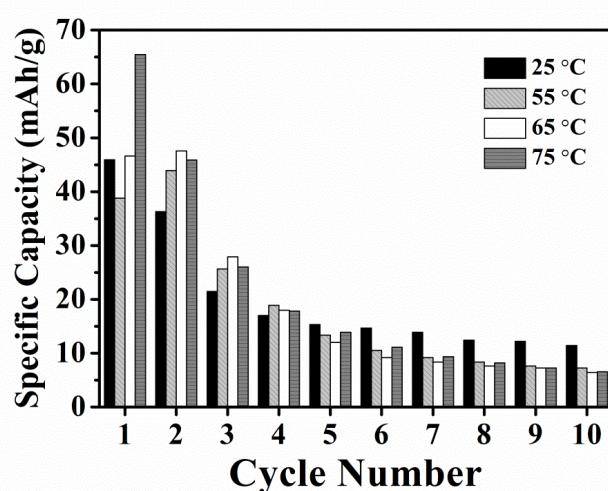
Compared with the MFS-H, a clear discharge platform appeared at 1.5 V. Note that this discharge platform does not only appear in the initial discharge curve, which confirms that this platform does not come from the generation of a solid electrolyte interphase (SEI) passivation layer. This result is attributed to the formation of an FeS<sub>2</sub> phase during the

sulfurization process for the ion battery. However, the theoretical capacity of pyrite is 894 mAh/g, and the amount of pyrite in the MFS-S lattices is merely ~1 wt.%, which indicates that the MFS-S lattices can serve as Li-ion hosts due to demagnesian in the first charge process.

Figure 13a displays the initial charge–discharge curve of MFS-S-900 at 75 °C. Compared to its capacity at room temperature, both the charge and discharge capacities increased remarkably at high temperature. This indicates that more ions participated in the insertion/extraction reaction in the active material. Figure 13b shows the MFS-S-900 cycling discharge capacities at the various temperatures. The MFS-S-900 has higher discharge capacities in 1~4 cycles at higher temperatures, which is attributed to a stronger ion diffusion-driving force. After 1~4 cycles, the discharge capacities of the working electrodes significantly deteriorate in 5~10 cycles. The retention rate of MFS-S is poor, which may attribute to the fact that FeS<sub>2</sub> cannot effectively serve as ion pathways with the huge volume change after lithiation/delithiation [27]. In addition, the high-temperature deterioration of PVDF, the dissolution of active material, and the increase in internal resistance may cause the deterioration of capabilities above 60 °C [28].



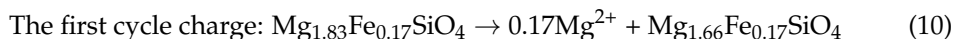
(a)



(b)

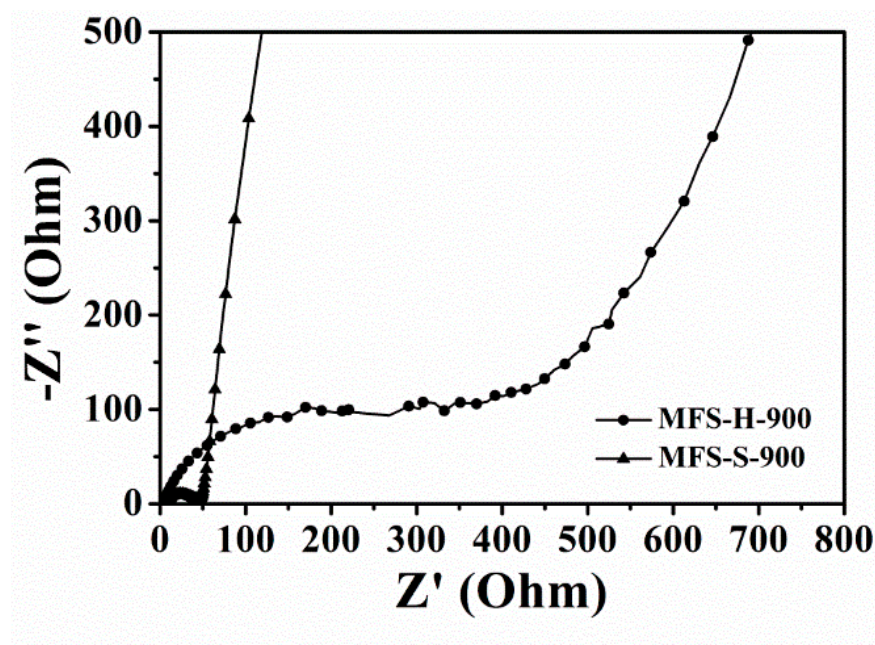
Figure 13. Capacity: (a) initial charge–discharge curve at 75 °C, (b) cycling discharge capacities at various temperatures for MFS-S-900.

The MFS-S electrochemical reactions can be written as Equations (10) and (11).



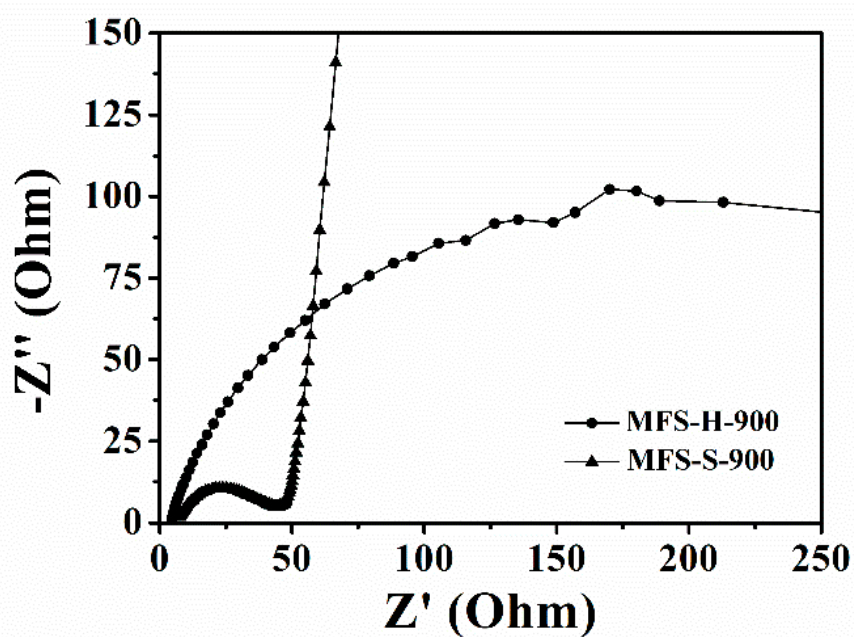
According to the initial charge–discharge curve and ICP-OES result, the  $\text{Mg}^{2+}$  ions were desorbed during the first charge cycle, which represents the formation of an  $\text{FeS}_2$  layer by the sulfidation, thus enhancing the surface crystallinity and conductivity of  $(\text{Mg, Fe})_2\text{SiO}_4$ . Moreover,  $\text{FeS}_2$  provides a channel for the extraction of  $\text{Mg}^{2+}$  ions from the  $(\text{Mg, Fe})_2\text{SiO}_4$  lattice, thus providing more insertion and extraction positions for Li ions in a subsequent charge and discharge process. Therefore, the capacitance of the MFS-S has a substantial increase compared to the MFS-H.

To understand the effects of sulfidation on the electrochemical system of the MFS-S, electrochemical impedance spectra (EIS) measurements were performed, as shown in Figure 14. In the high frequency region, the x-intercept represents the resistance caused from the electrolyte ( $R_s$ ). The semicircle in the intermediate frequency region is associated with the charge-transfer resistance ( $R_{ct}$ ) for ionic insertion/extraction on the electrode–electrolyte interface. According to the fitting results, the  $R_{ct}$  of MFS-S-900 is much lower than that of MFS-H-900, which indicates that the sulfidation reaction greatly enhances the electrical and ionic conductivities of MFS-S. The straight line in the low frequency region relates to the Warburg coefficient ( $\sigma$ ) being inversely proportional to the square root of the diffusion coefficient [15]; hence, the lower the Warburg coefficient, the higher the ionic mobility. According to Figure 14 and Table 3, it was found that ions and electrons can diffuse into the bulk material faster after forming a sulfidation layer.

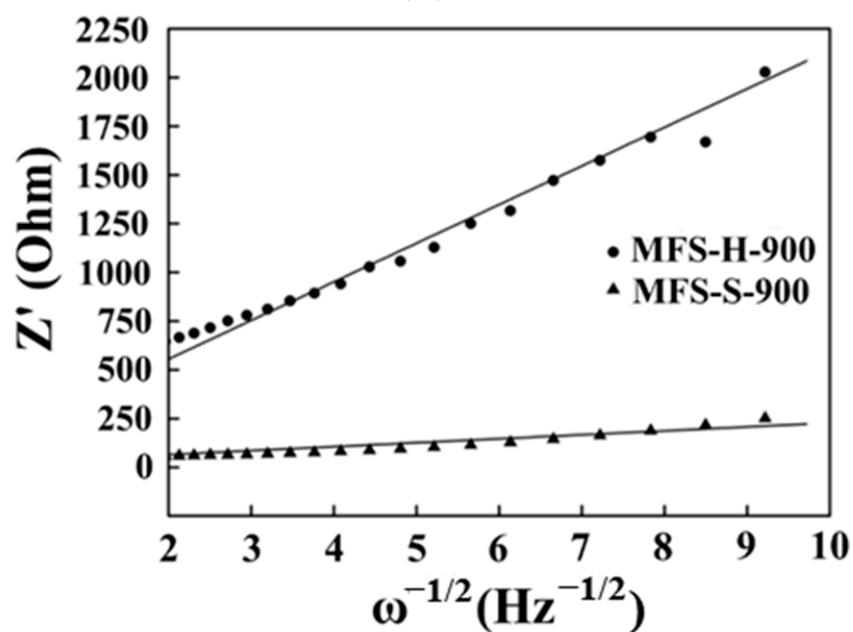


(a)

Figure 14. Cont.



(b)



(c)

**Figure 14.** Electrochemical impedance spectra: (a) full frequency, (b) mid-high frequency region, (c) plot for  $Z'$  vs.  $\omega^{-1/2}$  in the low frequency region for MFS-H-900 and MFS-S-900.

**Table 3.** Fitting results of EIS.

Categories	$R_s$ ( $\Omega$ )	$R_{ct}$ ( $\Omega$ )	$\sigma$ ( $\Omega\text{Hz}^{1/2}$ )
MFS-H-900	4.62	586.49	198.12
MFS-S-900	7.40	47.95	20.30

The initial discharge capacity of MFS-S-900 is 65.45 mAh/g at 75 °C. It is worth noting that the electrochemical properties of  $\text{FeS}_2$  at elevated temperatures differ from those at

room temperature, leading to battery deterioration. Despite the decrease in capacitance contributed by  $\text{FeS}_2$  at high temperatures, the elevated temperature enhances the driving force for magnesium ions and lithium ions to intercalate and desorb within the magnesium iron silicate lattice. Consequently, the gram capacitance at high temperatures still surpasses that at normal temperature. In this experiment, a thin layer of highly crystalline  $\text{FeS}_2$  was generated on the surface of magnesium iron silicate of serpentinite through sulfide sintering.  $\text{FeS}_2$  exhibits superior conductivity compared to ore powder and  $\text{Fe}_2\text{O}_3$ , thereby enhancing the surface crystallinity and conductivity of the powder. Moreover,  $\text{FeS}_2$  is used in lithium batteries and boasts excellent thermal stability. The  $\text{FeS}_2$  thin layer is less prone to deterioration at high temperatures, contributing to improve charge and discharge properties of magnesium iron silicate under elevated temperatures.

A schematic illustration of the charge–discharge mechanisms of MFS is presented in Figure 15. After forming a  $\text{FeS}_2$  layer on the serpentinite-derived magnesium iron silicate, the pyrite layer improved the surface crystallinity and conductivity without degrading at high temperature [29], and thus provided additional ion pathways, which is crucial to its application. Accordingly, serpentinite after the sulfidation process is eco-friendly and low-cost, and so deserves further development for application in the secondary battery.

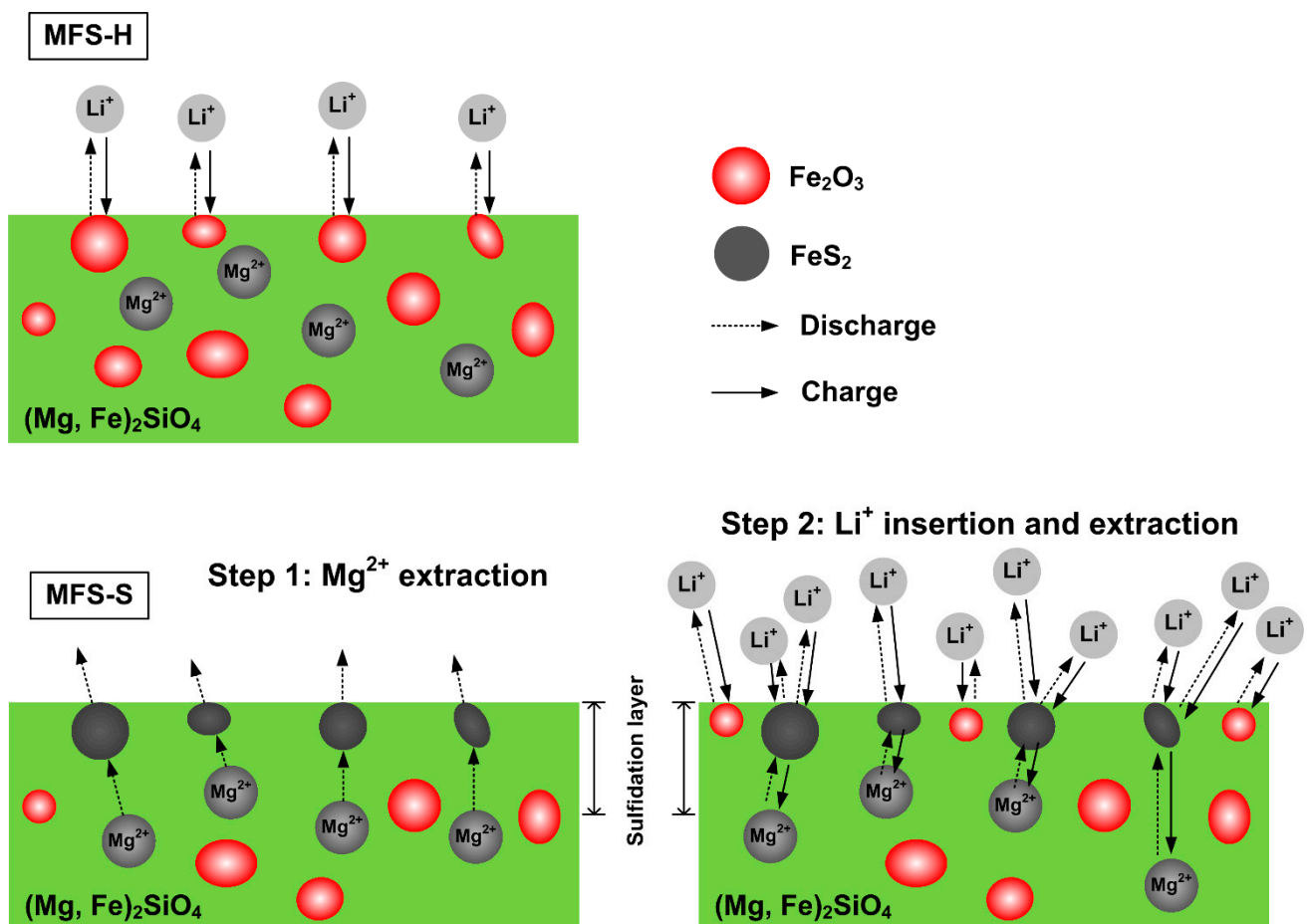


Figure 15. Schematic illustrations of the charge–discharge mechanisms of MFS.

#### 4. Limitation

While the surface modification of natural serpentinite powders presents promising potential for battery applications, certain limitations exist. The current study primarily focuses on the initial stages of research, and practical application in real battery systems requires further exploration and optimization. Furthermore, subsequent research could explore the utilization of natural serpentinite powders as components in solid electrolytes, particularly

in combination with polymers. This innovative approach aligns with the broader goals of energy conservation and carbon reduction, aiming to create environmentally friendly and sustainable battery technologies.

## 5. Conclusions

In this study, natural serpentinite powder underwent sulfidation, leading to the development of magnesium iron silicate (MFS) batteries. The transformation of serpentinite into magnesium iron silicate with good crystallinity occurred at a sintering temperature of 900 °C. However, the electrochemical properties were found to be suboptimal due to the low crystallinity of the surface.

Through low-vacuum sulfidation treatment, the MSF-S obtained from natural serpentinite exhibited high crystallinity in the interior and FeS<sub>2</sub> on the surface, which provided additional ion pathways, contributing to improved electrochemical performance. Notably, the FeS<sub>2</sub> layer remained intact even at high temperatures, enhancing the high-temperature charge–discharge properties of magnesium iron silicate.

The findings of this study affirm that MSF-S exhibits high-temperature applicability, high safety standards, and environmentally friendly characteristics. This research lays the groundwork for further exploration and utilization of natural serpentinite-derived materials in advanced battery technologies.

**Author Contributions:** Conceptualization, J.-R.Z.; Validation, K.-J.C. and P.-T.W.; Formal analysis, K.-J.C.; Investigation, J.-R.Z. and Y.-Y.T.; Resources, F.-Y.H.; Data curation, J.-R.Z.; Writing—original draft, Y.-Y.T.; Writing—review & editing, J.-R.Z., K.-J.C., F.-Y.H. and P.-T.W.; Supervision, F.-Y.H. All authors have read and agreed to the published version of the manuscript.

**Funding:** The authors are grateful to the Instrument Center of National Cheng Kung University and Minis-try of Science and Technology of Taiwan (NSTC 111-2221-E-006-061-MY2) for their financial support.

**Data Availability Statement:** Data are contained within the article.

**Conflicts of Interest:** The authors declare no conflict of interest.

## References

1. Watanabe, A.; Yamamoto, K.; Orikasa, Y.; Masese, T.; Mori, T.; Uchiyama, T.; Matsunaga, T.; Uchimoto, Y. Reaction mechanism of electrochemical insertion/extraction of magnesium ions in olivine-type FePO<sub>4</sub>. *Solid State Ionics* **2020**, *349*, 115311. [[CrossRef](#)]
2. Truong, Q.D.; Kobayashi, H.; Nayuki, K.; Sasaki, Y.; Honma, I. Atomic-scale observation of phase transition of MgMn<sub>2</sub>O<sub>4</sub> cubic spinel upon the charging in Mg-ion battery. *Solid State Ionics* **2020**, *344*, 115136. [[CrossRef](#)]
3. Callegari, D.; Colombi, S.; Nitti, A.; Simari, C.; Nicotera, I.; Ferrara, C.; Mustarelli, P.; Pasini, D.; Quartarone, E. Quartarone, Autonomous self-healing strategy for stable sodium-ion battery: A case study of black phosphorus anodes. *ACS Appl. Mater. Interfaces* **2021**, *13*, 13170–13182. [[CrossRef](#)] [[PubMed](#)]
4. Huang, Z.-D.; Masese, T.; Orikasa, Y.; Mori, T.; Yamamoto, K. Vanadium phosphate as a promising high-voltage magnesium ion (de)-intercalation cathode host. *RSC Adv.* **2015**, *5*, 8598–8603. [[CrossRef](#)]
5. Tarascon, J.-M.; Armand, M. Issues and challenges facing rechargeable lithium batteries. *Nature* **2001**, *414*, 359–367. [[CrossRef](#)] [[PubMed](#)]
6. Zhan, Y.; Zhang, W.; Lei, B.; Liu, H.; Li, W. Recent development of Mg ion solid electrolyte. *Front. Chem.* **2020**, *8*, 125. [[CrossRef](#)] [[PubMed](#)]
7. Aurbach, D.; Weissman, I.; Gofer, Y.; Levi, E. Nonaqueous magnesium electrochemistry and its application in secondary batteries. *Chem. Rec.* **2003**, *3*, 61–73. [[CrossRef](#)]
8. Dompablo, M.A.-D.; Armand, M.; Tarascon, J.; Amador, U. On-demand design of polyoxianionic cathode materials based on electronegativity correlations: An exploration of the Li<sub>2</sub>MSiO<sub>4</sub> system (M = Fe, Mn, Co, Ni). *Electrochem. Commun.* **2006**, *8*, 1292–1298. [[CrossRef](#)]
9. Zhou, F.; Cococcioni, M.; Kang, K.; Ceder, G. The Li intercalation potential of LiMPO<sub>4</sub> and LiMSiO<sub>4</sub> olivines with M = Fe, Mn, Co, Ni. *Electrochem. Commun.* **2004**, *6*, 1144–1148. [[CrossRef](#)]
10. Li, Y.; Nuli, Y.; Yang, J.; Yilinuer, T.; Wang, J. MgFeSiO<sub>4</sub> prepared via a molten salt method as a new cathode material for rechargeable magnesium batteries. *Chin. Sci. Bull.* **2011**, *56*, 386–390. [[CrossRef](#)]
11. NuLi, Y.; Zheng, Y.; Wang, F.; Yang, J.; Minnett, A.I.; Wang, J.; Chen, J. MWNT/C/Mg<sub>1.03</sub>Mn<sub>0.97</sub>SiO<sub>4</sub> hierarchical nanostructure for superior reversible magnesium ion storage. *Electrochem. Commun.* **2011**, *13*, 1143–1146. [[CrossRef](#)]

12. Zheng, Y.; NuLi, Y.; Chen, Q.; Wang, Y.; Yang, J.; Wang, J. Magnesium cobalt silicate materials for reversible magnesium ion storage. *Electrochimica Acta* **2012**, *66*, 75–81. [[CrossRef](#)]
13. Zhao, J.-R.; Wang, I.-H.; Hung, F.-Y. A New Secondary Battery Technology: Electrode Structure and Charge–Discharge Mechanism of All-Solid-State Zinc-Graphite Batteries. *Mater. Sci. Eng. B* **2024**, *299*, 116975. [[CrossRef](#)]
14. Kiyoura, R.; Ito, Y. Study on Thermal Transformation in the Synthetic and Natural Serpentine, especially Exothermic Reaction of Serpentine. *J. Ceram. Assoc. Jpn.* **1953**, *61*, 525. [[CrossRef](#)]
15. Lin, X.; Wang, P.; Li, P.; Yu, H.; Qian, S.; Shui, M.; Wang, D.; Long, N.; Shu, J. Improved the lithium storage capability of BaLi<sub>2</sub>Ti<sub>6</sub>O<sub>14</sub> by electroless silver coating. *Electrochimica Acta* **2015**, *186*, 24–33. [[CrossRef](#)]
16. Shih, Y.-T.; Wu, C.-H.; Hung, F.-Y.; Lui, T.-S.; Chen, L.-H. A study at room temperature and 55 °C on the charge–discharge characteristics of Si<sub>(100-x)</sub>Al<sub>x</sub> thin film anode for Li-ion batteries. *Surf. Coat. Technol.* **2013**, *215*, 79–84. [[CrossRef](#)]
17. Maxwell, J.C. Ophiolites—Ancient oceanic lithosphere?: R.G. Coleman. Springer, Berlin, 1977, 229 pp., DM 68.00 or US \$ 30.00. *Mar. Geol.* **1979**, *30*, 322–324. [[CrossRef](#)]
18. Jafari, A.; Shayesteh, S.F.; Salouti, M.; Boustani, K. Effect of annealing temperature on magnetic phase transition in Fe<sub>3</sub>O<sub>4</sub> nanoparticles. *J. Magn. Magn. Mater.* **2015**, *379*, 305–312. [[CrossRef](#)]
19. Jia, L.; Ashtiani, S.; Liang, F.; He, G.; Jiang, H. Hydrogen permeation through dual-phase ceramic membrane derived from automatic phase-separation of SrCe<sub>0.50</sub>Fe<sub>0.50</sub>O<sub>3-δ</sub> precursor. *Int. J. Hydrogen Energy* **2020**, *45*, 4625–4634. [[CrossRef](#)]
20. Palayangoda, S.S.; Nguyen, Q.P. Thermal behavior of raw oil shale and its components. *Oil Shale* **2015**, *32*, 160. [[CrossRef](#)]
21. Deng, J.; Wen, S.; Chen, X.; Xian, Y.; Wu, D. Dynamic Simulation of the Thermal Decomposition of Pyrite Under Vacuum. *Met. Mater. Trans. A* **2014**, *45*, 2445–2452. [[CrossRef](#)]
22. Sweeney, R.E.; Kaplan, I.R. Pyrite Framboid Formation; Laboratory Synthesis and Marine Sediments. *Econ. Geol.* **1973**, *68*, 618–634. [[CrossRef](#)]
23. Luther, G.W. Pyrite synthesis via polysulfide compounds. *Geochim. Cosmochim. Acta* **1991**, *55*, 2839–2849. [[CrossRef](#)]
24. Ouertani, B.; Ouerfelli, J.; Saadoun, M.; Bessaïs, B.; Ezzaouia, H.; Bernède, J. Characterization of FeS<sub>2</sub>-pyrite thin films synthesized by sulphuration of amorphous iron oxide films pre-deposited by spray pyrolysis. *Mater. Charact.* **2005**, *54*, 431–437. [[CrossRef](#)]
25. Ouertani, B.; Ouerfelli, J.; Saadoun, M.; Bessaïs, B.; Hajji, M.; Kanzari, M.; Ezzaouia, H.; Hamdadou, N.; Bernède, J. Transformation of amorphous iron oxide films pre-deposited by spray pyrolysis into FeS<sub>2</sub>-pyrite films. *Mater. Lett.* **2005**, *59*, 734–739. [[CrossRef](#)]
26. Brindley, G.W.; Hayami, R. Kinetics and Mechanisms of Dehydration and Recrystallization of Serpentine—I. *Clays Clay Miner.* **1963**, *12*, 35–47. [[CrossRef](#)]
27. Tran, D.T.; Dong, H.; Walck, S.D.; Zhang, S.S. Pyrite FeS<sub>2</sub>-C composite as a high capacity cathode material of rechargeable lithium batteries. *RSC Adv.* **2015**, *5*, 87847–87854. [[CrossRef](#)]
28. Bodenes, L.; Naturel, R.; Martinez, H.; Dedryvère, R.; Menetrier, M.; Croguennec, L.; Pérès, J.-P.; Tessier, C.; Fischer, F. Lithium secondary batteries working at very high temperature: Capacity fade and understanding of aging mechanisms. *J. Power Source* **2013**, *236*, 265–275. [[CrossRef](#)]
29. Shao-Horn, Y.; Osmialowski, S.; Horn, Q.C. Reinvestigation of Lithium Reaction Mechanisms in FeS<sub>2</sub> Pyrite at Ambient Temperature. *J. Electrochem. Soc.* **2002**, *149*, A1547–A1555. [[CrossRef](#)]

**Disclaimer/Publisher’s Note:** The statements, opinions and data contained in all publications are solely those of the individual author(s) and contributor(s) and not of MDPI and/or the editor(s). MDPI and/or the editor(s) disclaim responsibility for any injury to people or property resulting from any ideas, methods, instructions or products referred to in the content.